Nano Research

Open Access

Research Article

High responsivity and fast speed n-$MoSe_2$/p-GeSn/n-GOI phototransistor with a composition-graded GeSn base for short-wave infrared photodetection

Xinwei Cai§, Jiaxin Qin§, Huiling Pan, Li Jiang, Tianwei Yang, Rui Wang, Jiayi Li, Guangyang Lin ✉, Songyan Chen, Wei Huang, and Cheng Li ✉

College of physical science and technology, Semiconductor Photonics Research Center, Xiamen University, Xiamen 361005, China
§ Xinwei Cai and Jiaxin Qin contributed equally to this work.

Cite this article: *Nano Research*, **2025**, *18*, 94907335. https://doi.org/10.26599/NR.2025.94907335

ABSTRACT: In this work, a short-wave infrared (SWIR) n-$MoSe_2$/p-GeSn/n-germanium-on-insulator (GOI) heterojunction phototransistor (HPT) with Sn composition-graded GeSn base is proposed for improvement of overall performance at low cost. The Sn composition-graded GeSn base layers are grown using magnetron sputtering epitaxy technique for improvement of crystal quality with a high Sn content of 15.2% in the top layer, rendering the extension of the cutoff wavelength beyond 2400 nm and significant suppression of dark current. The enormous electron/hole injection ratio, resulting from the large bandgap offset between the $MoSe_2$ emitter and the GeSn base, enables the harvesting of a high photocurrent gain of HPT. By optimizing the device parameters, a considerable responsivity of 23.79 A/W and an excellent specific detectivity of 8.24 × 10^{10} Jones at the peak wavelength of 2030 nm were achieved for the HPT with the dark current density of 261 mA/cm² under the emitter-collector bias voltage of 1.0 V at room temperature. The fast response speed is obtained for the HPT in terms of rising/falling times of 2.8 μs/9.3 μs at 1550 nm, surpassing those of most van der Waals (vdW) junction-based devices. Those results demonstrate that GeSn HPTs are suitable for SWIR optoelectronic imaging and microwave photonics applications.

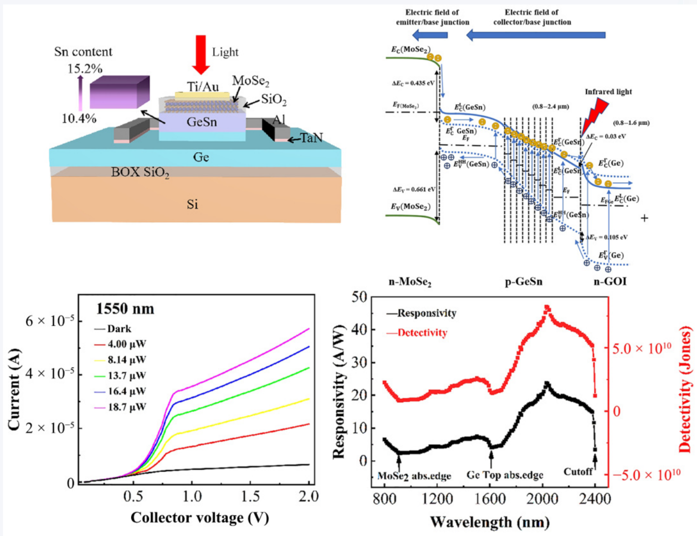

KEYWORDS: composition-graded GeSn layers, $MoSe_2$, magnetron sputtering technique, van der Waals heterojunction, short-wave infrared, phototransistor

1 Introduction

Short-wave infrared (SWIR) imaging systems play a crucial role in various modern technological applications, particularly in medical diagnostics, industrial monitoring, radio-over-fiber interconnection, and national defense [1, 2]. Specifically, since SWIR light in 2–2.5 μm band falls between the absorption bands of atmospheric H_2O molecules [3], and CO_2 exhibits distinct spectral fingerprints near 1.6 and 2.1 μm, these absorption peaks lie within water absorption windows of varying intensities [3]. Imaging systems operating in this band hold significant importance in fields like astronomical observation and weather forecasting. Currently, the mainstream commercial SWIR optoelectronic imaging systems mainly use photodetectors (PDs) based on Group III–V (InGaAs, InSb etc.) and Group II–VI (HgCdTe) materials as detection units [4–6]. Although these PDs show promising performance in SWIR detection, their drawbacks, including low operating temperature and incompatibility with standard complementary metal-oxide-semiconductor (CMOS) technology, significantly increase the

Received: December 17, 2024; **Revised:** January 26, 2025
Accepted: February 26, 2025

✉Address correspondence to Cheng Li, lich@xmu.edu.cn; Guangyang Lin, gylin@xmu.edu.cn

complexity and costs of their applications. In contrast, Group-IV semiconductor materials have outstanding prospects in the field of photodetection due to their low-cost and capability for large-scale integration [7]. However, traditional Group-IV materials, such as silicon (Si) and germanium (Ge), have indirect bandgaps and absorption edge of less than 1600 nm, which severely hinder their applications in SWIR detection. Recently, germanium tin (GeSn), as an emerging Group IV material, has attracted significant attention due to its tunable bandgap energy (from 0.66 to 0 eV) with different Sn contents and strain levels, ability to turn into a direct bandgap material with enhanced band-to-band light absorption as Sn content reaches above 8%, and high compatibility with CMOS technology [8–11]. More importantly, GeSn alloy could be epitaxially grown on Si substrates at low growth costs for high integration capability, making it a promising light-absorbing material for detection units in the next generation of SWIR optoelectronic imaging systems.

In recent years, GeSn-based optoelectronic devices have gradually garnered attention and research, and various types of GeSn PDs for SWIR photodetection have been reported, including p-i-n PDs, metal-semiconductor-metal (MSM) PDs, photoconductors, avalanche photodiodes (APDs), and phototransistors. Relatively low responsivity near 2 μm is always feathered for p-i-n photodiodes due to the thickness constrain of GeSn thin films compromised by crystal quality and Sn fraction [12, 13]. While the nature of high surface state density of GeSn makes it challenging to suppress dark current and improve specific detectivity of MSM PDs [14]. To improve the performance of GeSn PDs in 2 μm band, photoconductors, APDs, and phototransistors have been explored to enhance responsivities with high photocurrent gain. Among them, photoconductors are notable for their simple structure and high responsivity, but the long response time and requirement of low operating temperature (77 K) extremely reduce their practicability [15]. APDs have the advantage of being able to operate at room temperature, however, they often suffer from high breakdown voltages and significant noise [16]. Compared to those devices, phototransistors can operate at room temperature and offer advantages such as lower operating voltage, reduced noise, and higher photocurrent gain. In 2020, Hung et al. reported a first phototransistor based on $Ge_{0.951}Sn_{0.049}$ with an extended cutoff wavelength of 2 μm [17]. However, the device demonstrated low specific detectivity and a photocurrent gain of less than 5, primarily due to the insufficient carrier injection ratio provided by the Ge homojunction serving as emitter-base junction. To achieve higher photocurrent gain, a proposed alternative strategy involves replacing the homojunction with a heterojunction.

Two-dimensional (2D) materials, particularly 2D transition metal dichalcogenides (TMDs), have garnered significant attention due to their unique physical properties, excellent optoelectronic performance, and compatibility with mature Si CMOS technology [18–20]. Furthermore, 2D flakes can easily be integrated with other dimensional materials to form van der Waals (vdW) heterostructures, and effectively circumventing the lattice mismatch issues. Previously, we have proposed and demonstrated an n-$MoSe_2$/p-$Ge_{0.829}Sn_{0.171}$/n-Ge HPT with a large responsivity of 12.75 A/W as well as an outstanding specific detectivity of 1.74×10^{10} Jones at 2250 nm [21]. However, its performance still has substantial room for improvement, as indicated by the large dark current density in the order of A/cm^2 and the long response time in the order of hundreds of microseconds.

Herein, in order to suppress the dark current and improve response speed of the GeSn HPT, we propose the Sn composition-graded GeSn layers as base on a germanium-on-insulator (GOI) substrate. The improved quality of Sn composition-graded GeSn layers and graded potential profile in the base region significantly suppress the dark current by one order of magnitude and decrease the response time to microseconds. The large band gap offset between n-$MoSe_2$ emitter and p-GeSn base provides enormous electron/hole injection ratio, rendering high photocurrent gain. In addition, the buried SiO_2 layer of the GOI substrate and the top dielectric layer of device form an optical resonant cavity, further enhancing the responsivity and photocurrent gain of the HPT at some certain wavelength. The overall photoelectric performance of the proposed n-$MoSe_2$/p-GeSn/n-GOI HPT would be greatly improved.

2 Experimental

2.1 Materials and device fabrication

The GeSn epilayers were grown on an n-GOI substrate, featuring an approximately 200 nm-thick Ge top layer with the doping concentration of about 1×10^{18} cm^{-3}, using low-cost high-temperature magnetron sputtering epitaxy technique. Before growing the GeSn layers, the GOI substrate underwent successive cleaning with acetone, ethyl alcohol, and deionized water in an ultrasonic bath. After that, the surface oxides were etched by immersing the substrate sequentially in diluted hydrochloric acid solution, hydrofluoric acid solution, and deionized water, followed by spin-drying. Then the cleaned n-GOI substrate was mounted on a stainless-steel holder and loaded into the sputtering chamber with a base pressure of 5.0×10^{-5} Pa. Prior to the growth of GeSn, the GOI substrate was heated to 471 °C and intrinsic 5N Ge targets were sputtered with a DC power of 68.6 W for 300 s to deposit a 100 nm-thick Ge buffer layer on the GOI substrate under a pressure of 0.5 Pa in Ar (5N purity) environment. After that, temperature was reduced to 294 °C for the growth of Sn composition-graded GeSn layers. The sputtering power of Sn target was remained at 6.72 W, while the DC sputtering power of the intrinsic 5N Ge target was gradually adjusted from 68.6 to 60.9 W by ten steps. This adjustment enabled the co-sputtering and growth of Sn-composition-graded, unintentionally doped GeSn epilayers. The $MoSe_2$ flakes were mechanically exfoliated from bulk $MoSe_2$ and then transferred onto a SiO_2/Si substrate with a 300 nm SiO_2 top layer.

After the preparation of all the materials, the mechanically exfoliated $MoSe_2$ flakes were stacked on the GeSn epilayers by wet transfer method. The n-$MoSe_2$/p-GeSn heterojunction was then annealed in a vacuum oven at 100 °C for 10 min to improve the contact interface, followed by depositing a 100 nm-thick SiO_2 protective layer with plasma-enhanced chemical vapor deposition (PECVD). Next, a square mesa (50 μm × 50 μm) encompassing the selected $MoSe_2$ flake was defined using maskless laser lithography. The remaining SiO_2 and GeSn areas were then etched away with buffered oxide etchant (BOE) and $HCl:H_2O_2:H_2O$ (1:1:10) solution. Atomic layer deposition (ALD) and PECVD were then used to grow 30 nm-thick Al_2O_3 and 250 nm-thick SiO_2 as the sidewall passivation layer and isolation layer, respectively. After that, maskless laser lithography and BOE solution were used to define and etch electrode contact windows on the $MoSe_2$ and n-GOI substrate. Magnetron sputtering was employed to deposit 10 nm

Ti/100 nm Au and 10 nm TaN/100 nm Al as their contact electrodes, respectively. The TaN layer was used to alleviate Fermi-level pinning (FLP) effect on the surface of the n-GOI substrate for ohmic contacts [22]. Finally, the device underwent rapid thermal annealing (RTA) at 300 °C for 3 min to improve electrode contact.

2.2 Materials and device characterizations

Atomic force microscopy (AFM) and scanning electron microscopy (SEM) were selected to characterize the surface morphology and thickness of GeSn epilayers, respectively, while X-ray diffraction (XRD) was tested to determine the crystalline quality. The thickness of $MoSe_2$ flakes was also estimated by AFM, and a laser confocal Raman spectrometer (WITec alpha 300RA) with 532 nm exciting laser was employed to identify the Raman characteristic lines of the $MoSe_2$ flakes.

The electrical characteristics of HPTs were measured by the electrical testing system consisting of a Semishare probe station, Keithley 2611B and 2635B source meters, and a light-isolated black box. The optoelectronic performance of the HTP was characterized by the optical testing system, primarily comprising a halogen tungsten light source, a monochromator, fiber-coupled laser diodes (1064, 1310, and 1550 nm), an oscilloscope, a microscopic focusing system with an incident light path, and a signal generator.

During the measurement of response spectrum, a halogen tungsten light source was employed to generate mixed-wavelength light (the relationship of halogen tungsten lamp's light power density with the wavelength of light can be seen in the Fig. S1 in the Electronic Supplementary Material (ESM)). The light entered the monochromator through slits, then it was dispersed by internal gratings. The dispersed monochromatic light exited the monochromator and was coupled into the incident light path of the microscopic focusing system via an optical fiber, then vertically projected onto the surface of device.

3 Results and discussion

3.1 Device structure and characterization of materials

The three-dimensional (3D) schematic view and the optical microscope image of the n-$MoSe_2$/p-GeSn/n-GOI HPT are shown in Figs. 1(a) and 1(b), respectively. The n-GOI substrate serves as the collector, and the p-GeSn epilayer acts as the base, while the n-$MoSe_2$ flakes, transferred to the surface of the GeSn epilayers to form vdW heterojunction, function as the emitter. The quality of GeSn layers is effectively improved with gradually increase of Sn composition, therefore significantly reduces the background hole concentration to 1×10^{17} cm^{-3} in the unintentionally doped GeSn layers [23]. The inset in Fig. 1(a) shows the Sn contents of GeSn epilayers gradually rise from 10.4% of the bottom layer to 15.2% of the top layer. The details on growth and characterization of the Sn composition-graded GeSn layers can be referred to our previous work [24]. The depletion width of collector-base junction is increased mainly in the slightly-doped base region along with the heavy doping in the n-Ge top layer of GOI substrate. This would result in short transit time for photogenerated carriers passing through the base with reduction of recombination of the electron current injected from the emitter within the neutral region of the base. The optimum design and technology are expected to render significant improvement of photocurrent gain and response times of the HPT.

The $MoSe_2$ flakes and $MoSe_2$/GeSn heterojunction were characterized using an optical microscope, AFM, and Raman spectroscopy, as shown in Figs. 1(c)–1(e). In Fig. 1(d) of AFM image, the thickness of selected $MoSe_2$ flake is approximately 80 nm. In Fig. 1(e), the Raman spectra of the isolated GeSn and $MoSe_2$ films each display a single peak: the A_{1g} mode of $MoSe_2$ at around 241.1 cm^{-1} and the LO mode of GeSn at around 292 cm^{-1}. The Raman spectrum of the $MoSe_2$/GeSn heterojunction includes both peaks of $MoSe_2$ and GeSn, confirming the successful assembly of the vdW heterojunction.

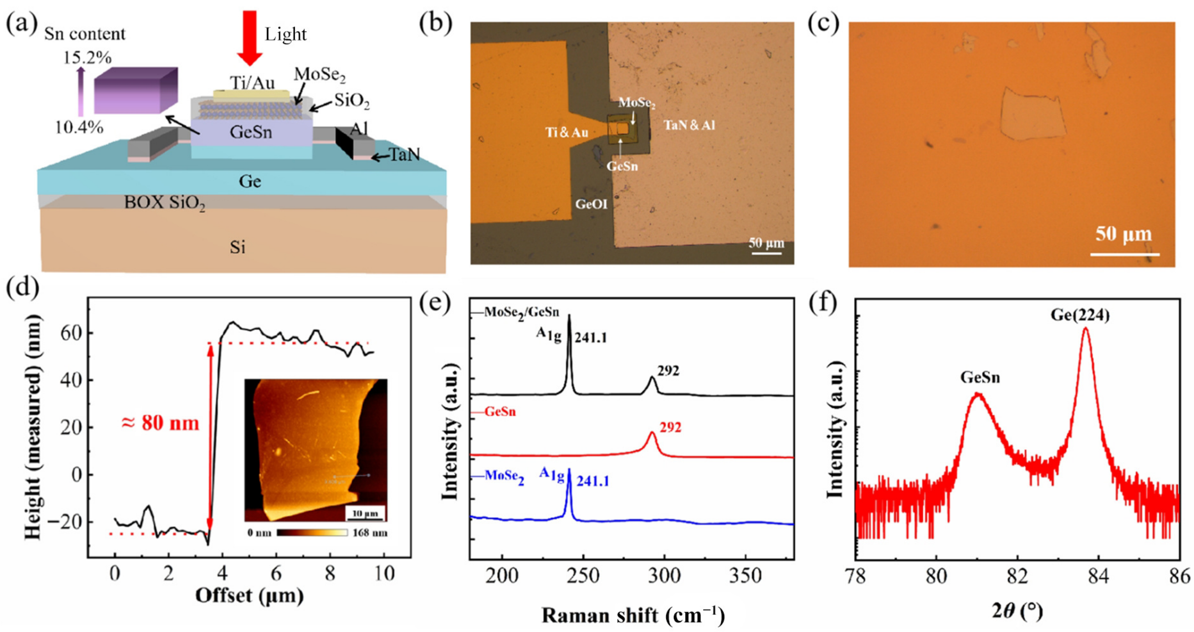

Figure 1 (a) The 3D schematic view of the proposed device. The inset shows the Sn composition-graded of the GeSn epilayer changing from 10.4% of the bottom layer to 15.2% of the top layer. (b) The top view under an optical microscope after fabrication of the n-$MoSe_2$/p-GeSn/n-GOI HPT device. (c) The optical microscope image of $MoSe_2$/GeSn heterojunction. (d) Thickness profile of $MoSe_2$ taken by AFM. (e) Typical Raman spectra of the GeSn, $MoSe_2$ film, and $MoSe_2$/GeSn heterojunction. (f) The XRD (224) rocking curve of GeSn taken from ω–2θ scan.

Figure 1(f) shows the (224) XRD ω–2θ rocking curve of the Sn composition-graded GeSn epilayers. The asymmetric shape and broad GeSn peak indicate the variation of Sn content and strain relaxation of the GeSn epilayer, as inferred in our previous work (the XRD-RSM (224) of GeSn epilayers is shown in Fig. S2 in ESM) [24].

3.2 Electrical and photo-response characteristics

To further understand the optoelectronic performance of the n-$MoSe_2$/p-GeSn/n-GOI HPT, this section characterizes the output characteristic curves, response spectrum, and response times of the device under illumination. The responsivities, specific detectivities, photocurrent gains, and response speeds are then calculated and analyzed based on these measurements. The output characteristic curves of the HPT in amplification modes were measured under 1064, 1310, and 1550 nm wavelength illumination, as illustrated in Figs. 2(a)–2(c), respectively. The photocurrent increases strongly with the incident power, obviously separated from the dark current, showing typical output characteristics of the bipolar phototransistor. According to these curves, the responsivities (R) and specific detectivities (D^*) can be calculated by the following equations [25]

$$R = \frac{I_{\mathrm{ph}}}{P_{\mathrm{in}}} \tag{1}$$

$$D^* = \frac{R\left(A \times \Delta f\right)^{1/2}}{\left(i_{\mathrm{n}}^2\right)^{1/2}} \tag{2}$$

where I_{ph} is photocurrent, P_{in} is the incident light power, A is photosensitive area, Δf is bandwidth of PD, i_{n} is the noise current. If the noise current (i_{n}) is dominated by the shot noise (i_{shot}), it can be expressed as $i_{\mathrm{shot}} = (2qI_{\mathrm{D}}\Delta f)^{1/2}$ [26, 27], where q is electron charge, and I_{D} is the dark current of PD. Hence, D^* can be simplified as

$$D^* = \frac{RA^{1/2}}{\left(2qI_{\mathrm{D}}\right)^{1/2}} \tag{3}$$

The dependence of calculated R and D^* on the incident light powers at 1064, 1310, and 1550 nm for the HPT under $V_{\mathrm{CE}} = 2$ V are shown in Figs. 2(d)–2(f), respectively. Under 1064, 1310, and 1550 nm illumination, the n-$MoSe_2$/p-GeSn/n-GOI HPT achieved maximum responsivities of 2.9, 5.58, and 3.79 A/W, and specific detectivities of 1×10^{10}, 1.93×10^{10}, and 1.31×10^{10} Jones, respectively. The dark current density of the HPT under a positive collector-emitter bias of 2 V (in amplification mode) is about 261 mA/cm^2, which is much better than most of Ge-based HPTs. The lower dark current can be attributed to the improvement of crystal quality of Sn composition-graded GeSn epilayers and the resultant graded electron potential distribution in this region. We notice that the responsivity of the HPT slightly decreases with the increase of incident light power. This could be attributed to the photogenerated-carrier-induced narrowing of depletion region in the base on the side of base-collector junction, which increases the

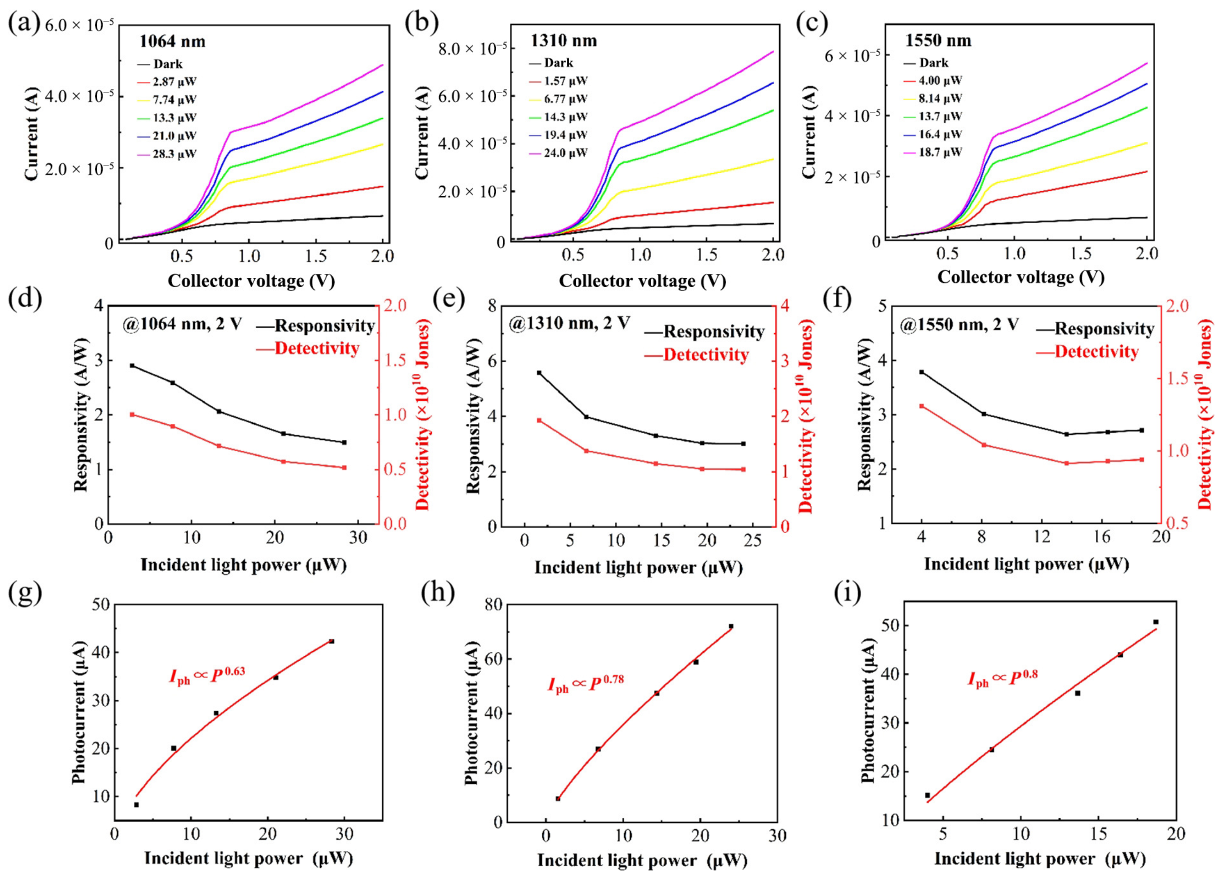

Figure 2 The output characteristic curves of the n-$MoSe_2$/p-GeSn/n-GOI HPT in amplification mode under illumination at wavelengths of (a) 1064 nm, (b) 1310 nm, and (c) 1550 nm, as well as the corresponding responsivities and specific detectivities at different incident light powers ($V_{\mathrm{CE}} = 2$ V) for (d) 1064 nm, (e) 1310 nm, and (f) 1550 nm. The relationship between I_{ph} ($V_{\mathrm{CE}} = 2$ V) and P under illumination at (g) 1064 nm, (h) 1310 nm, and (i) 1550 nm.

probability of carrier recombination in the base and thus reduces the responsivity.

To further evaluate the photoresponse characteristics, the photocurrent I_{ph} (at V_{CE} = 2 V) under illumination at wavelengths of 1064, 1310, and 1550 nm was fitted to the incident light power P by the power function $I_{ph} \propto AP^{\alpha}$, as shown in Figs. 2(g)–2(i), respectively. The sublinear relationship between I_{ph} and P indicates that the density of photogenerated carriers is positively correlated with the absorbed light. The power exponents α extracted at 1064, 1310, and 1550 nm are 0.63, 0.78, and 0.8, respectively, implying the loss of photoexcited carriers during the transport. This can be attributed to the large valence band offset between $MoSe_2$ and GeSn that restrict the transport of photogenerated carriers, and the recombination in the neutral region of the base. The improvement of power exponent α can be attributed to the enhancement of built-in electrical field at the base-collector junction and the reduction of width of neutral base region.

To further understand the detection performance of the n-$MoSe_2$/p-GeSn/n-GOI HPT device in NIR-SWIR bands, the response spectrum and specific detectivity (D^*) under V_{CE} = 1 V from 800 to 2400 nm were measured at room temperature and shown in Fig. 3. The photoresponse spectrum of the device exhibits three distinct absorption edges, corresponding to the absorption edges of $MoSe_2$ at around 900 nm, Ge at around 1600 nm, and the cutoff wavelength of 2400 nm (limited by the light source). Due to high Sn contents in the Sn composition-graded GeSn epilayers, the optical absorption of device was primarily effective beyond 2 μm, resulting in higher responsivity in this wavelength range. Notably, a significant response peak was observed at 2030 nm for the n-$MoSe_2$/p-GeSn/n-GOI HPT, which might be attributed to the optical modulation of the resonant cavity formed by the buried SiO_2 of the GOI substrate and the top dielectric layer (the reflectance spectrum of this HPT calculated by Matlab software can be seen in the Fig. S3 in the ESM). Under an applied bias of V_{CE} = 1 V, the n-$MoSe_2$/p-GeSn/n-GOI HPT achieves a peak responsivity of 23.79 A/W and a specific detectivity of 8.24 × 10^{10} Jones at 2030 nm. At 2250 nm, the responsivity of HPT reaches about 18.36 A/W, and the specific detectivity is approximately 6.36 × 10^{10} Jones. Those results demonstrate that the proposed HPT owns excellent performance in 1.6–2.4 μm bands, compared with most of GeSn photodetectors reported previously.

To evaluate the photo-current gain of the n-$MoSe_2$/p-GeSn/n-GOI HPT, a p-GeSn/n-GOI photodiode was also fabricated on the same n-GOI substrate with the identical active materials and mesa size, except the $MoSe_2$ flakes. The response spectrum of this p-GeSn/n-GOI PD in the 800–2400 nm wavelength range was measured (see Fig. S4 in the ESM for details). The photocurrent gain G can be calculated as [28]

$$G = \frac{I_{ph}}{I_p} \quad (4)$$

where I_p is the primary photocurrent measured from the referenced p-GeSn/n-GOI PD, and I_{ph} is the photocurrent of the n-$MoSe_2$/p-GeSn/n-GOI HPT under identical incident light power with considering the loss of reflection. To evaluate the photocurrent gain, the reflection spectra for these two devices were simulated by Matlab software as shown in Fig. S3 in the ESM, and the photocurrent of the HPT can be evaluated by $I_{ph} = I_{ph0}P_{in}P_D/P_{in\ HPT} = I_{ph0}(1 - Re_{PD})/(1 - Re_{HPT})$, where I_{ph0} is the measured photocurrent of HPT, $P_{in\ PD}$ and $P_{in\ HPT}$ are the incident light powers of PD and HPT, respectively, while Re_{HPT} and Re_{PD} are the reflectances of HPT and PD, respectively. According to these results, we finally calculated that the photocurrent gain G of the n-$MoSe_2$/p-GeSn/n-GOI HPT is about 48.4 and 63.7 at wavelengths of 2030 and 2250 nm, respectively [21].

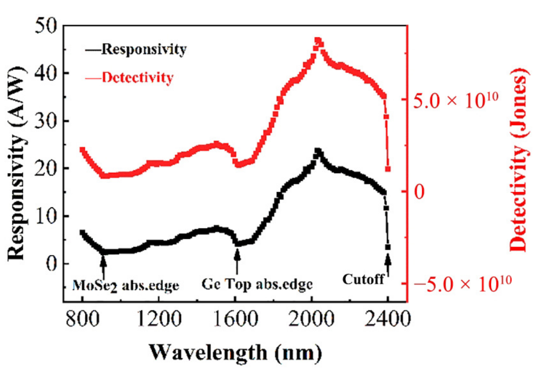

Figure 3 Responsivity (the left coordinate axis) and detectivity (the right coordinate axis) of the n-$MoSe_2$/p-GeSn/n-GOI HPT under V_{CE} = 1 V for wavelengths between 800 and 2400 nm.

To understand the operating mechanism of the two-terminal n-$MoSe_2$/p-GeSn/n-GOI HPT, Figs. 4(a) and 4(b) depict the band alignment diagrams of the device. Figure 4(a) illustrates the band diagram of the HPT under thermal equilibrium, while Fig. 4(b) shows the transport of photogenerated carriers under illumination ranging from 0.8 to 2.4 μm. For the Sn composition-graded GeSn epilayers, the direct and indirect band gaps were calculated by the 30-band k·p model. The band structure mainly consists of the heavy-hole valence band at Γ valley (E_v^{HH}(GeSn)), the minimum of the conduction band at Γ valley (E_c^{Γ}(GeSn)), and the minimum of the conduction band at L valley (E_c^{L}(GeSn)). The indirect band gap of the top GeSn layer is approximately 0.465 eV, the direct band gap is around 0.304 eV, and the electron affinity is about 4.345 eV. The bottom GeSn layer has an indirect band gap of about 0.526 eV, a direct band gap of approximately 0.566 eV, and an electron affinity of about 4.159 eV. Under thermal equilibrium, the Fermi levels of n-$MoSe_2$, the Sn composition-graded p-GeSn layers, and the n-GOI would align, resulting in the band diagram of the device (the solid line represents the minimum of the conduction band at L valley, while the dashed line represents the minimum of the conduction band at Γ valley and the heavy-hole valence band), as shown in Fig. 4(a). The bent region of the band structure between the emitter-base and collector-base junctions generates the built-in electric fields indicated by blue arrows. Regarding the emitter-base junction, the band offset between n-$MoSe_2$ and the top layer of p-GeSn is approximately 0.435 eV for the conduction band and 0.661 eV for the valence band, resulting in a band gap difference of about 1.096 eV. According to Eq. (5) [29]

$$\frac{i_{ne}}{i_{pe}} = \frac{D_n L_p N_D}{D_p L_n N_A}\left(\frac{m_{p(P)} m_{n(P)}}{m_{p(N)} m_{n(N)}}\right)^{3/2} \exp\left(\frac{\Delta E_g}{kT}\right) \quad (5)$$

where i_{ne} and i_{pe} are the electron current and the hole current of the HPT's emitter-base junction at a forward bias voltage, respectively; D_n (D_p) and L_n (L_p) are the diffusion coefficient and diffusion length of electrons (holes), respectively; N_D and N_A represent the doping concentration in the n-$MoSe_2$ and p-GeSn, respectively; $m_{p(P)}$ ($m_{n(P)}$) and $m_{p(N)}$ ($m_{n(N)}$) stand for the effective masses of holes (electrons) in p-type base and n-type emitter, respectively; k is the Boltzmann constant, T is room temperature, and ΔE_g is the bandgap difference between n-$MoSe_2$ and p-GeSn. The

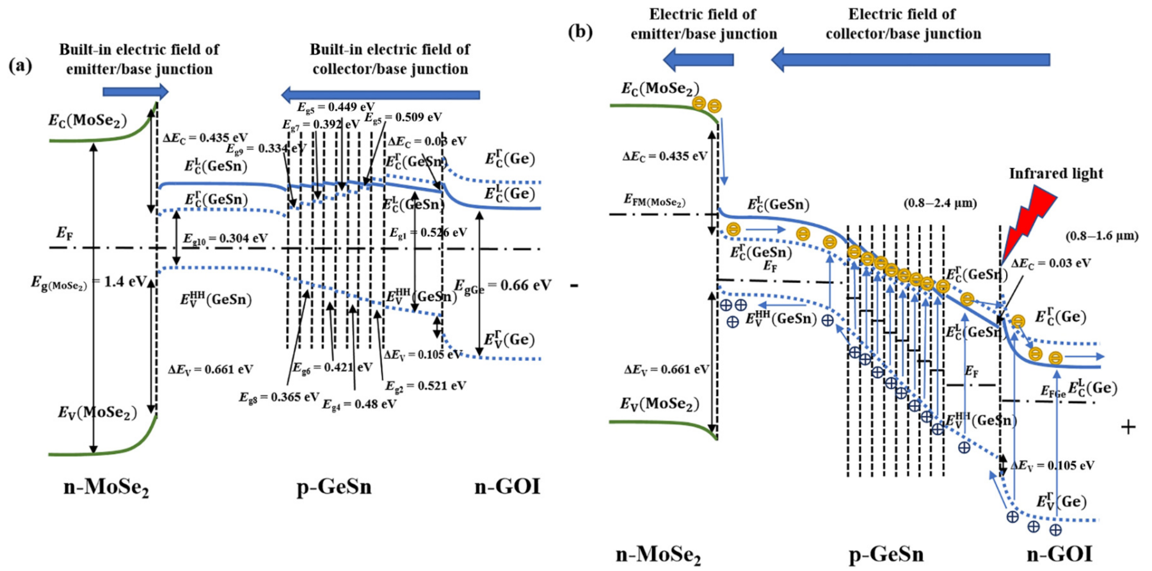

Figure 4 (a) Energy band alignment of n-$MoSe_2$/p-GeSn/n-GOI HPT in thermal equilibrium. (b) Photo-induced carrier's transportation of HPT in amplification mode under illumination for the wavelength of light ranges from 0.8 to 2.4 μm.

electron/hole current injection ratio of the emitter-base junction is estimated to be 10^{18}, theoretically allowing the n-$MoSe_2$/p-GeSn/n-GOI HPT to generate substantial photocurrent gain. When the device operates in amplification mode ($V_{CE} > 0$) and illuminated with light ranging from 0.8 to 2.4 μm, the transport process of photogenerated carriers is illustrated in Fig. 4(b). In the band of 0.8 to 1.6 μm, the incidence can be absorbed by both the Sn composition-graded p-GeSn epilayers in the base region and the top layer of Ge in the collector region of n-GOI. In the wavelength range of 1.6 to 2.4 μm, the incident light can be only absorbed by the Sn-composition-graded p-GeSn epilayers in the base region. Upon excitation by incident light, the photogenerated electron-hole pairs are separated by the electrical field at the base-collector junction, with electrons entering the Ge collector region and being collected by the electrode. Due to the large band offset between n-$MoSe_2$ and the top layer of p-GeSn (emitter-base junction), photogenerated holes transport and accumulate at the base region near the emitter-base junction, lowering the barrier height and significantly enhancing the electron injection from n-$MoSe_2$ into the p-GeSn base region, thereby enabling the device to exhibit large photocurrent gain. While working in dark environment, the current that outflows from the emitter (I_E) of HPT can be calculated as [21]: $I_E = (1 + \beta)\, I_{CBO}$, where β is the common emitter current gain and I_{CBO} is the dark current of collector junction. According to the Eq. (5), the large band gap difference between $MoSe_2$ and GeSn improves current gain, which would also amplify reverse leakage dark current at the collector junction. To minimize the dark current while preserving the photocurrent gain as much as possible, it is crucial to reduce the reverse current produced by the collector junction.

Response time is the other critical parameter of the n-$MoSe_2$/p-GeSn/n-GOI HPT, which can be evaluated by periodically illuminating the device with wavelengths of 1064, 1310, and 1550 nm under a collector-emitter bias voltage of 2 V. The rising/falling times of this device are shown in Figs. 5(a)–5(f). The rising (falling) times under pulsed illumination at 1064, 1310, and 1550 nm are 3.4 μs (7.7 μs), 3.3 μs (10.5 μs), and 2.8 μs (9.3 μs), respectively. It is noteworthy that photodiodes based on vdW heterojunctions usually exhibit long photo response times, typically in the order of milliseconds or even seconds, due to the trapping of photo-induced carriers at the heterojunction interface [30, 31]. In this case, the vdW heterojunction serves as emitter-base junction of HPT, which represents a significant improvement of carrier transit times.

A comparison of the optoelectronic performance parameters between the n-$MoSe_2$/p-GeSn/n-GOI HPT in this work, our previously reported n-$MoSe_2$/p-GeSn/n-Ge HPT, and some other typical high-performance GeSn photodetectors reported in recent years are shown in Table 1. Compared to traditional GeSn photodetectors, our designed GeSn-based vdW HPT exhibits a larger photocurrent gain. The HPTs can operate at room temperature under low bias conditions, with considerably high responsivity, specific detectivity, and short response time. This approach provides valuable reference for the design and fabrication of high-performance GeSn photodetectors that can be integrated into SWIR optoelectronic imaging systems.

4 Conclusions

In summary, a two-terminal n-$MoSe_2$/p-GeSn/n-GOI vdW HPT was proposed and demonstrated for SWIR detection. The Sn composition-graded GeSn epilayers with a top Sn content of 15.2% were grown by magnetron sputtering technique on an n-GOI substrate with a doping concentration of 1×10^{18} cm^{-3}, serving as the base of the HPT. As a result, the HPT exhibits low dark current density and extended detection wavelength in the range of 800–2400 nm. The large bandgap difference between the n-$MoSe_2$ emitter and the p-GeSn base renders ultrahigh electron/hole injection ratio of 10^{18}, thus providing very high photocurrent gain when operating in amplification mode ($V_{CE} > 0$). Very high responsivities of 23.79 and 18.36 A/W, and substantial specific detectivities of 8.24×10^{10} and 6.36×10^{10} Jones at 2030 and 2250 nm, respectively, are achieved for the n-$MoSe_2$/p-GeSn/n-GOI HPT under a collector-emitter bias of 1 V at room temperature. The photocurrent gains are estimated to be 48.4 and 63.7 at 2030 and 2250 nm, respectively, with a dark current density of only 261 mA/cm^2 and response time of several microseconds. This work provides an effective strategy to design and fabricate high

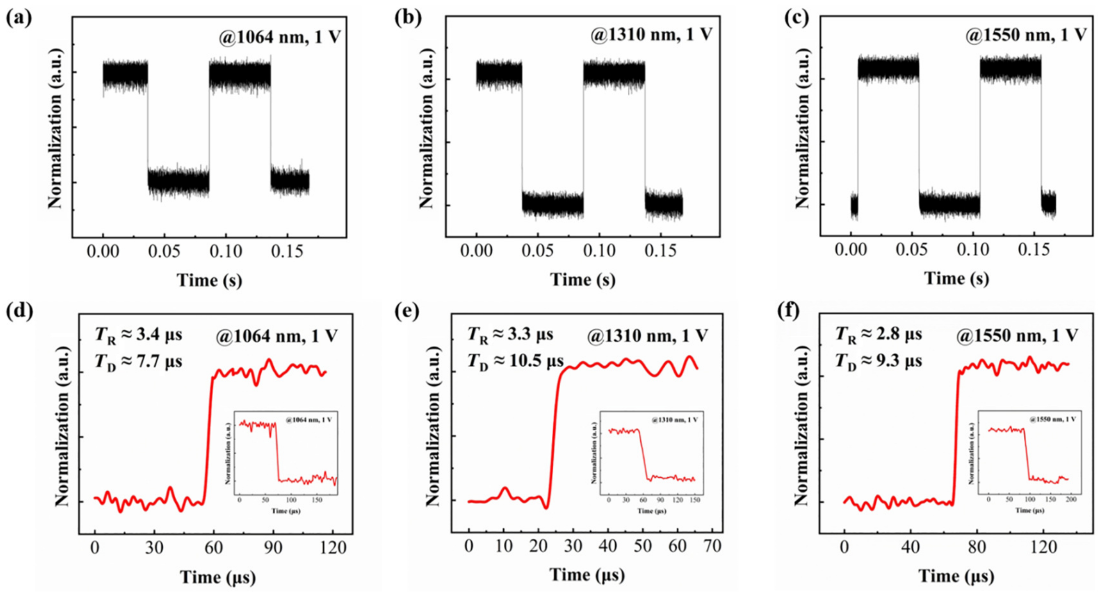

Figure 5 The response times under pulsed illumination of n-$MoSe_2$/p-GeSn/n-GOI HPT at (a) 1064 nm, (b) 1310 nm, and (c) 1550 nm, and the rising/falling times at (d) 1064 nm, (e) 1310 nm, and (f) 1550 nm (at $V_{CE} = 2$ V).

Table 1 Comparison of device performances for n-$MoSe_2$/p-GeSn/n-GOI HPT in this work, our previous reported n-$MoSe_2$/p-GeSn/n-Ge HPT and other reported typical GeSn-based PDs

Device	Sn content	Cutoff wavelength (nm)	Responsivity (A/W)	Detectivity (Jones)	Refs.
$MoSe_2$/GeSn/GOI HPT	15.2% (max)	2400	23.79@2030 nm	8.24×10^{10}	This work
$MoSe_2$/GeSn/Ge HPT	17.1%	2400	12.75@2250 nm	1.74×10^{10}	[21]
GeSn PIN photodiode	11%	2650	0.32@2000 nm	1.7×10^{9}	[12]
GeSnOI MSM photodetector	9%	2200	0.06@2003 nm	—	[13]
GeSn photoconductor	12.5% (max)	2650	16.1@2000 nm, 77 K	1.1×10^{10}@77 K	[15]
GeSn photoconductor	16.3	4200	0.35@2530 nm, 77 K	9.33×10^{8}@77 K	[32]
GeSn MQW photodiode	8%	2260	0.11@2000 nm	2.137×10^{8}	[12]
p^+-Ge/n-Ge/GeSn/p-Ge HPT	4.9%	1940	0.68@1550 nm	—	[17]

performance GeSn-based PDs for SWIR photodetection, showing promising application prospects in fields like astronomical observation, weather forecasting, military targeting, and so on.

Electronic Supplementary Material: Supplementary material (the relationship of halogen tungsten lamp's light power density with the wavelength of light which generates mixed-wavelength light measuring the response spectrum of HPT; the reflection spectra of the HPT and the control device (without $MoSe_2$) simulated using Matlab software; the response spectrum of p-GeSn/n-GOI photodetector with the same mesa area without $MoSe_2$ flakes in 800–2400 nm wavelength range) is available in the online version of this article at https://doi.org/10.26599/NR.2025.94907335.

Data availability

All data needed to support the conclusions in the paper are presented in the manuscript and the Electronic Supplementary Material. Additional data related to this paper may be requested from the corresponding author upon request.

Acknowledgements

This work was supported in part by the National Natural Science Foundation of China (Nos. 62074134 and 62104205) and in part by the National Key Research and Development Program of China (No. 2018YFB2200103).

Declaration of competing interest

All the contributing authors report no conflict of interests in this work.

Author contribution statement

X. W. C.: Data curation, formal analysis, investigation, methodology, visualization, writing – original draft, writing – review & editing. J. X. Q.: Data curation, formal analysis, investigation, methodology, validation, writing – review & editing. H. L. P.: Formal analysis, methodology, resources. L. J.: Formal analysis, methodology, resources. T. W. Y.: Formal analysis, methodology, resources. R. W.: Formal analysis, methodology, resources. J. Y. L.: Formal analysis, methodology, resources. G. Y. L.: Formal analysis, investigation, supervision, writing – review & editing. S. Y. C.: Formal analysis, investigation, supervision. W. H.: Formal analysis, investigation, supervision. C. L.: Conceptualization, funding acquisition, resources, supervision, writing – review & editing. All the authors have approved the final manuscript.

Use of AI statement

None.

References

[1] Martyniuk, P.; Antoszewski, J.; Martyniuk, M.; Faraone, L.; Rogalski, A. New concepts in infrared photodetector designs. *Appl. Phys. Rev.* **2014**, *1*, 041102.

[2] . Grönwall, C.; Hamoir, D.; Steinvall, O.; Larsson, H.; Amselem, E.; Lutzmann, P.; Repasi, E.; Göhler, B.; Barbé, S.; Vaudelin, O. et al. Measurements and analysis of active/passive multispectral imaging. In *Proceedings of Electro-Optical Remote Sensing, Photonic Technologies, and Applications VII*; *and Military Applications in Hyperspectral Imaging and High Spatial Resolution Sensing*, Dresden, Germany, 2013, pp 889705.

[3] Zhang, Y. G.; Gu, Y.; Shao, X. M.; Li, X.; Gong, H. M.; Fang, J. X. Short-wave infrared InGaAs photodetectors and focal plane arrays. *Chin. Phys. B* **2018**, *27*, 128102.

[4] . Yuan, H.; Zhang, J. W.; Kim, J.; Bond, D.; Laquindanum, J.; Kimchi, J.; DeForest, M. G. Recent progress in extended wavelength InGaAs photodetectors and comparison with SWIR HgCdTe photodetectors. In *Proceedings of Infrared Sensors, Devices, and Applications IX*, San Diego, USA, 2019, pp 111290E.

[5] Bakarov, A. K.; Gutakovskii, A. K.; Zhuravlev, K. S.; Kovchavtsev, A. P.; Toropov, A. I.; Burlakov, I. D.; Boltar', K. O.; Vlasov, P. V.; Lopukhin, A. A. MBE-grown InSb photodetector arrays. *Tech. Phys.* **2017**, *62*, 915–919.

[6] Rogalski, A. HgCdTe infrared detector material: History, status and outlook. *Rep. Prog. Phys.* **2005**, *68*, 2267–2336.

[7] Soref, R.; Buca, D.; Yu, S. Q. Group IV photonics: Driving integrated optoelectronics. *Opt. Photon. News* **2016**, *27*, 32–39.

[8] Shimura, Y.; Wang, W.; Vandervorst, W.; Gencarelli, F.; Gassenq, A.; Roelkens, G.; Vantomme, A.; Caymax, M.; Loo, R. $Ge_{1-x}Sn_x$ optical devices: Growth and applications. *ECS Trans.* **2014**, *64*, 677–687.

[9] Gong, X.; Dong, Y.; Xu, S. Q.; Wang, W. Germanium-tin ($Ge_{1-x}Sn_x$) photodetectors for 2 μm wavelength band. *Jpn. J. Appl. Phys.* **2021**, *60*, SB0805.

[10] D'Costa, V. R.; Cook, C. S.; Birdwell, A. G.; Littler, C. L.; Canonico, M.; Zollner, S.; Kouvetakis, J.; Menéndez, J. Optical critical points of thin-film $Ge_{1-y}Sn_y$ alloys: A comparative Ge_{1-y}Sny/Ge_{1-x}Six study. *Phys. Rev. B* **2006**, *73*, 125207.

[11] Fang, C. Z.; Liu, Y.; Zhang, Q. F.; Han, G. Q.; Gao, X.; Yao, S.; Zhang, J. C.; Hao, Y. Germanium-tin alloys: Applications for optoelectronics in mid-infrared spectra. *Opto-Electron Adv.* **2018**, *1*, 180004.

[12] Zhou, H.; Xu, S. Q.; Lin, Y. D.; Huang, Y. C.; Son, B.; Chen, Q. M.; Guo, X.; Lee, K. H.; Goh, C. K.; Gong, X. et al. High-efficiency GeSn/Ge multiple-quantum-well photodetectors with photon-trapping microstructures operating at 2 μm. *Opt. Express* **2020**, *28*, 10280–10293.

[13] Li, X. L.; Peng, L. Z.; Liu, Z.; Zhou, Z. Q.; Zheng, J.; Xue, C. L.; Zuo, Y.; Chen, B.; Cheng, B. 30 GHz GeSn photodetector on SOI substrate for 2 μm wavelength application. *Photon. Res.* **2021**, *9*, 494–500.

[14] Son, B.; Lin, Y. D.; Lee, K. H.; Margetis, J.; Kohen, D.; Tolle, J.; Tan, C. S. Metal-semiconductor-metal photodetectors on a GeSn-on-insulator platform for 2 μm applications. *IEEE Photon. J.* **2022**, *14*, 6824406.

[15] Tran, H.; Pham, T.; Margetis, J.; Zhou, Y. Y.; Dou, W.; Grant, P. C.; Grant, J. M.; Al-Kabi, S.; Sun, G.; Soref, R. A. et al. Si-based GeSn photodetectors toward mid-infrared imaging applications. *ACS Photon.* **2019**, *6*, 2807–2815.

[16] . Zhang, D. L.; Hu, X. Y.; Liu. D. C.; Lin, X.; Wang, W. P.; Ding, Z. Y.; Wang, Z. Q.; Cheng, B. W.; Xue, C. L. GeSn on Si avalanche photodiodes for short wave infrared detection. In *Proceedings of Optical Sensing and Imaging Technologies and Applications*, Beijing, China, 2018, pp 108461B.

[17] Hung, W. T.; Barshilia, D.; Basu, R.; Cheng, H. H.; Chang, G. E. Silicon-based high-responsivity GeSn short-wave infrared heterojunction phototransistors with a floating base. *Opt. Lett.* **2020**, *45*, 1088–1091.

[18] Novoselov, K. S.; Geim, A. K.; Morozov, S. V.; Jiang, D.; Zhang, Y.; Dubonos, S. V.; Grigorieva, I. V.; Firsov, A. A. Electric field effect in atomically thin carbon films. *Science* **2004**, *306*, 666–669.

[19] Zheng, W.; Liu, X. H.; Xie, J. Y.; Lu, G. C.; Zhang, J. Emerging van der Waals junctions based on TMDs materials for advanced gas sensors. *Coord. Chem. Rev.* **2021**, *447*, 214151.

[20] Duan, X. D.; Wang, C.; Pan, A. L.; Yu, R. Q.; Duan, X. F. Two-dimensional transition metal dichalcogenides as atomically thin semiconductors: Opportunities and challenges. *Chem. Soc. Rev.* **2015**, *44*, 8859–8876.

[21] Cai, X. W.; Li, S.; Qian, J. H.; Ding, H. K.; Wu, S. S.; Wang, R.; Wu, Q.; Shentu X. W.; Lin, G. Y.; Li, C. High-performance N-$MoSe_2$/P-GeSn/N-Ge van der Waals heterojunction phototransistor for short-wave infrared photodetection. *Adv. Optical Mater.* **2023**, *12*, 2301724.

[22] Wang, J. Y.; Huang, W.; Xu, J. F.; Li, J.; Huang, S. H.; Li, C.; Chen, S. Y. Schottky barrier height modulation effect on n-Ge with TaN contact. *Mater. Sci. Semicond. Process.* **2019**, *91*, 206–211.

[23] Markevich, V. P.; Peaker, A. R.; Hamilton, B.; Litvinov, V. V.; Pokotilo, Y. M.; Lastovskii, S. B.; Coutinho, J.; Carvalho, A.; Rayson, M. J.; Briddon, P. R. Tin-vacancy complex in germanium. *J. Appl. Phys.* **2011**, *109*, 083705.

[24] Qin, J. X.; Cai, X. W.; Pan, H. L.; Yang, T. W.; Chen, S. Y.; Huang, W.; Lin, G. Y.; Li, C. Low-cost high-performance p-GaSe/i-GeSn/n-GOI heterojunction photodiode for visible to short-wave infrared multispectral detection. *IEEE Electron Device Lett.* **2024**, *45*, 2443–2446.

[25] Mao, Y. C.; Xu, P. P.; Wu, Q.; Xiong, J.; Peng, R. M.; Huang, W.; Chen, S. Y.; Wu, Z. Y.; Li, C. Self-powered high-detectivity lateral MoS_2 Schottky photodetectors for near-infrared operation. *Adv. Electron. Mater.* **2021**, *7*, 2001138.

[26] Wang, F.; Wang, Z. X.; Xu, K.; Wang, F. M.; Wang, Q. S.; Huang, Y.; Yin, L.; He, J. Tunable GaTe-MoS_2 van der Waals p-n junctions with novel optoelectronic performance. *Nano Lett.* **2015**, *15*, 7558–7566.

[27] Lan, Z. J.; Lei, Y. L.; Edward Chan, W. K.; Chen, S. M.; Luo, D.; Zhu, F. R. Near-infrared and visible light dual-mode organic photodetectors. *Sci. Adv.* **2020**, *6*, eaaw8065.

[28] Chang, Y. H.; Zhang, W. J.; Zhu, Y. H.; Han, Y.; Pu, J.; Chang, J. K.; Hsu, W. T.; Huang, J. K.; Hsu, C. L.; Chiu, M. H. et al. Monolayer $MoSe_2$ grown by chemical vapor deposition for fast photodetection. *ACS Nano* **2014**, *8*, 8582–8590.

[29] Kroemer, H. Theory of a wide-gap emitter for transistors. *Proc. IRE* **1957**, *45*, 1535–1537.

[30] Hekmatikia, A.; Abdi, Y. Graphene-Silicon-based high-sensitivity and broadband phototransistor. *IEEE Electron Device Lett.* **2018**, *39*, 216–219.

[31] Shin, G. H.; Park, C.; Lee, K. J.; Jin, H. J.; Choi, S. Y. Ultrasensitive phototransistor based on WSe_2-MoS_2 van der Waals heterojunction. *Nano Lett.* **2020**, *20*, 5741–5748.

[32] Liu, X. Q.; Zheng, J.; Niu, C. Q.; Liu, T. R.; Huang, Q. X.; Li, M. M.; Zhang, D. D.; Pang, Y. Q.; Liu, Z.; Zuo, Y. H. et al. Sn content gradient GeSn with strain controlled for high performance GeSn mid-infrared photodetectors. *Photon. Res.* **2022**, *10*, 1567–1574.